










Strong [O III] $\lambda 5007$ Compact Galaxies Identified from SDSS DR16 and Their Scaling Relations

Weiyu Ding^{1,2,3} , Hu Zou³ , Xu Kong^{1,2} , Yulong Gao^{4,5} , Fujia Li^{1,2} , Hongxin Zhang^{2,6}, Jiali Wang³, Jie Song^{1,2} , Jipeng Sui³, Jundan Nie³ , Suijian Xue³, Weijian Guo³, Yao Yao^{1,2}, and Zhimin Zhou³

¹ Deep Space Exploration Laboratory / Department of Astronomy, University of Science and Technology of China, Hefei 230026, People's Republic of China
xkong@ustc.edu.cn

² School of Astronomy and Space Science, University of Science and Technology of China, Hefei 230026, People's Republic of China

³ Key Laboratory of Optical Astronomy, National Astronomical Observatories, Chinese Academy of Sciences, Beijing 100012, People's Republic of China
zouhu@nao.cas.cn

⁴ School of Astronomy and Space Science, Nanjing University, Nanjing 210093, People's Republic of China

⁵ Key Laboratory of Modern Astronomy and Astrophysics (Nanjing University), Ministry of Education, Nanjing 210093, People's Republic of China

⁶ Department of Astronomy, University of Science and Technology of China, Hefei 230026, People's Republic of China

Received 2023 March 22; revised 2023 June 28; accepted 2023 July 17; published 2023 August 30

Abstract

Green-pea galaxies are a special class of star-forming compact galaxies with strong [O III] $\lambda 5007$ and considered as analogs of high-redshift Ly α -emitting galaxies and potential sources for cosmic reionization. In this paper, we identify 76 strong [O III] $\lambda 5007$ compact galaxies at $z < 0.35$ from DR16 of the Sloan Digital Sky Survey. These galaxies present relatively low stellar mass, high star-formation rate, and low metallicity. Both the star-forming main-sequence (SFMS) relation and mass–metallicity relation (MZR) are investigated and compared with green-pea and blueberry galaxies collected from literature. It is found that our strong [O III] $\lambda 5007$ compact galaxies share common properties with those compact galaxies with extreme star formation and show distinct scaling relations in respect to those of normal star-forming galaxies at the same redshift. The slope of SFMS is higher, indicates that strong [O III] $\lambda 5007$ compact galaxies might grow faster in stellar mass. The lower MZR implies that they may be less chemically evolved and hence on the early stage of star formation. A further environmental investigation confirms that they inhabit relatively low-density regions. Future large-scale spectroscopic surveys will provide more details on their physical origin and evolution.

Unified Astronomy Thesaurus concepts: [Emission line galaxies \(459\)](#); [Star formation \(1569\)](#); [Metallicity \(1031\)](#)

1. Introduction

In modern extragalactic astrophysics, one of the most significant topics is to understand main physical processes occurring during the epoch of reionization (EoR). In the early universe, the intergalactic medium (IGM) changed from being neutral and opaque to ionized and transparent. Reionization seems to have been completed by $z \sim 6$ (Fan et al. 2006; McGreer et al. 2015). Star-forming galaxies (SFGs; e.g., Robertson et al. 2010; Finkelstein et al. 2019; Yung et al. 2020), active galactic nuclei (AGNs; e.g., Haiman & Loeb 1998; Yung et al. 2021; Finkelstein & Bagley 2022), and quasars (e.g., Madau et al. 2004) are possible candidates for the source of the ionizing radiation. It is generally believed that star-forming galaxies are the main contributors to reionization. However, star-forming regions typically have a large volume of HI gas around them, which prevents the ionizing radiation emitted by hot stars from escaping into the IGM. If low- and intermediate-mass galaxies have a fully ionized interstellar medium or galaxies could be perforated by optically thin tunnels so that the ionizing radiation could escape, they may get around this problem (Nakajima & Ouchi 2014; Rivera-Thorsen et al. 2015). Although significant progress has been made over the past 5–10 yr, the production

and escape of ionizing radiation in star-forming galaxies have not been fully understood yet.

Due to the difficulty of observing high-redshift galaxies that leak Lyman-continuum radiation (LyC, $\lambda_{\text{rest}} < 912\text{\AA}$), it is critical to find some low-redshift analogies. Green-pea (GP) galaxies have many similarities with high-redshift SFGs, such as high specific star-formation rates and low metallicities (Izotov et al. 2011; Nakajima & Ouchi 2014; Henry et al. 2015). A significant proportion of GP galaxies show high LyC escape fractions ranging from 1% to 50% (Henry et al. 2015; Verhamme et al. 2017; Izotov et al. 2020). It makes GP galaxies crucial systems for studying the escape mechanism of ionizing radiation.

Green-pea galaxies were originally identified in the Galaxy Zoo project (Lintott et al. 2008) by citizen scientists. Following this discovery, Cardamone et al. (2009) used unique characteristics of compact size and green color caused by the strong [O III] $\lambda 5007$ emission line to discover the first sample of GP galaxies from the Sloan Digital Sky Survey (SDSS; York et al. 2000). A total of 251 GP galaxies from SDSS DR7 are discovered by color selection in the redshift range of $0.112 < z < 0.360$, among which only 80 of them have optical spectra. Different from the typical GP definition, Jiang et al. (2019) used the equivalent width of either [O III] $\lambda 5007$ or H β to obtain 800 GP-like galaxies from SDSS DR13. Brunner et al. (2020) used strong [O III] $\lambda 5007$ emission lines to find 13 GP galaxies in the redshift range of $0.29 < z < 0.41$ from the KPNO International Spectroscopic Survey (Salzer et al. 2000). Generally, green-pea galaxies are selected in a relatively



Original content from this work may be used under the terms of the [Creative Commons Attribution 4.0 licence](#). Any further distribution of this work must maintain attribution to the author(s) and the title of the work, journal citation and DOI.

narrow redshift range. However, blueberry and purple grape galaxies are thought to be essentially identical to GP galaxies, except that they are located in different redshift ranges (Liu et al. 2022). Blueberry galaxies are young starburst galaxies at $z < 0.05$ (Yang et al. 2017a). In this redshift range, the [O III] $\lambda 5007$ emission line is within g band, which makes their colors blue. As a contrast, GP galaxies in the redshift range of $0.112 < z < 0.36$ have the [O III] $\lambda 5007$ line within r band. Purple grape galaxies are those at $z > 0.36$ with [O III] $\lambda 5007$ within i band and the UV continuum redshifted to g band and are those at $0.05 < z < 0.112$ with both strong [O III] $\lambda 5007$ within the g band and $H\alpha$ within the i band.

In this paper, we intend to compile a catalog of galaxies with strong [O III] $\lambda 5007$ emission lines from SDSS DR16 (Ahumada et al. 2020) and explore their physical properties and scaling relations. The paper is organized as follows. In Section 2, we describe the data and sample selection criteria. In Section 3, we describe the measurements of physical properties for the galaxy sample. Section 4 presents the basic properties and scaling relations, including the star-forming main-sequence relation and mass–metallicity relation. Comparisons with other GP galaxies and GP-like galaxies from the literature are also shown in this section. Section 5 gives a summary. In this paper, we assume a Λ -CDM standard cosmology with $H_0 = 70 \text{ km s}^{-1} \text{ Mpc}^{-1}$, $\Omega_m = 0.3$, and $\Omega_\Lambda = 0.7$. All photometric magnitudes are in AB mag.

2. Data and Sample

2.1. Spectroscopic Data and Data Preprocessing

The spectroscopic data used in this paper are from the sixteenth data release (DR16; Ahumada et al. 2020) of the SDSS (York et al. 2000). DR16 includes the data of the extended Baryon Oscillation Spectroscopic Survey (eBOSS; Dawson et al. 2016) of SDSS IV (Blanton et al. 2017). The survey uses the Sloan Foundation 2.5 m Telescope at Apache Point Observatory (Gunn et al. 2006) and the BOSS spectrograph (Dawson et al. 2013), which has 1000 fibers per 7 deg^2 plate at a resolution of $R \sim 2000$ and covers the wavelength range of 3600–10000 Å. The eBOSS aims to study the expansion history of the universe by using different tracers of spectroscopic redshifts, including luminous red galaxies, emission line galaxies, and quasars. There are a total of 1.4 million spectra observed by the eBOSS (Ahumada et al. 2020), where about 860,000 galaxies and quasars are new with respect to previous data releases.

We choose the objects in DR16 with the spectroscopic classification of “GALAXY” and reliable redshift measurements. The spectral fitting code of STARLIGHT (Cid Fernandes et al. 2005) is used to derive the underlying stellar continuum for each galaxy. It is subtracted from the observed spectrum in order to measure intrinsic fluxes of emission lines generated from the gas. In STARLIGHT, we use single stellar populations from Bruzual & Charlot (2003) models, the Salpeter (1955) initial mass function (IMF) and the attenuation law of Calzetti et al. (2000). The fluxes of strong emission lines (e.g., $H\beta$, [O III] $\lambda 4959, 5007$, $H\alpha$, and [N II] $\lambda 6583$) are calculated by the Gaussian-profile fitting with an IDL package MPFIT (Markwardt 2009). Following the method of Ly et al. (2014), we also estimate the flux errors and signal-to-noise ratios (S/Ns). The gas-phase extinction is calculated using the Balmer decrement with the assumption of the intrinsic flux

ratio $(H\alpha/H\beta)_0 = 2.86$ under the case-B recombination. All the fluxes of emission lines are extinction-corrected with the Calzetti et al. (2000) attenuation curve.

2.2. Sample Selection

The strong [O III] $\lambda 5007$ compact galaxies are selected using the following criteria:

1. [O III] $\lambda 5007$ line is detected with flux S/N greater than 5;
2. [O III] $\lambda 5007$ line is strong enough, where its equivalent width is larger than 200 Å (Malkan et al. 2021);
3. The galaxy has a compact size, i.e., the radius containing 90% of the Petrosian flux in SDSS r band (PetroR90_r) is smaller than $3''$ (Jiang et al. 2019).

We obtain a total of 162 galaxies satisfying the above selection criteria in a redshift range of $z < 0.48$. These galaxies are visually examined with SDSS composite color images. It is found that quite a few galaxies appear to be a part of large galaxies (possibly H II regions, e.g., the rightmost panel of Figure 1) or contaminated by neighbors. Their photometry and corresponding properties could be considerably affected by host or nearby galaxies. A total of 85 galaxies are discarded.

To exclude galaxies with AGN activities, we apply the [N II]/ $H\alpha$ versus [O III]/ $H\beta$ diagnostic diagram (now known as the BPT diagram; Baldwin et al. 1981; Veilleux & Osterbrock 1987) to classify our galaxies into different spectral types according to the discrimination lines proposed by Kewley et al. (2001) and Kauffmann et al. (2003). The BPT diagram is shown in Figure 2. There are 76 galaxies classified as star-forming galaxies (red pentagrams), two galaxies as composite (green crosses), and seven galaxies as AGNs (purple diamonds). We are only concerned with star-forming galaxies, so AGNs are not analyzed in the rest of this paper. The clustering of galaxies in the top left of Figure 2 indicates that our star-forming galaxies have high-ionization intensity ratios and possibly have low metallicities.

We have finally chosen 76 galaxies in the redshift range of $0.02 < z < 0.35$. The first three panels in Figure 1 display the color images of three typical examples at different redshifts in our final sample. Figure 3 shows the galaxy distributions on two color–color diagrams. In this figure, we also show the green-pea galaxies from Cardamone et al. (2009) at $0.112 < z < 0.360$ in yellow triangles, and those from Yang et al. (2017a) at $0.098 < z < 0.34$ in gray diamonds. The black solid lines mark the color selection criteria from Cardamone et al. (2009). Many of our strong [O III] $\lambda 5007$ compact galaxies are located out of the color boxes proposed by Cardamone et al. (2009). Our galaxies have lower redshifts but approximate [O III] equivalent widths and sizes of GP galaxies, so they should be the local counterparts of such galaxies. The galaxy distribution in the color space could be used for defining new selection criteria of GP-like galaxies at $z < 0.35$.

3. Physical Properties of our Strong [O III] $\lambda 5007$ Compact Galaxies

3.1. Star-formation Rate

Strong emission lines are usually used to estimate the star-formation rate (SFR). Due to low redshifts of our galaxies, we adopt the most accurate SFR calibration based on the $H\alpha$

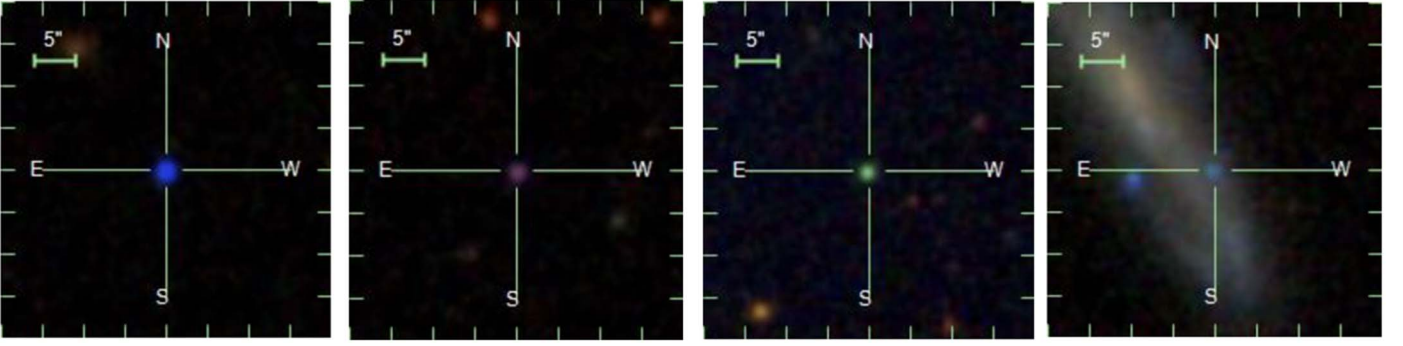


Figure 1. SDSS color images of some galaxies in our selected sample. The first three galaxies are GP-like compact galaxies at $z = 0.04, 0.09,$ and $0.22,$ respectively. The last panel shows a galaxy excluded by us through visual examination, which might be a star-formation region of a large galaxy.

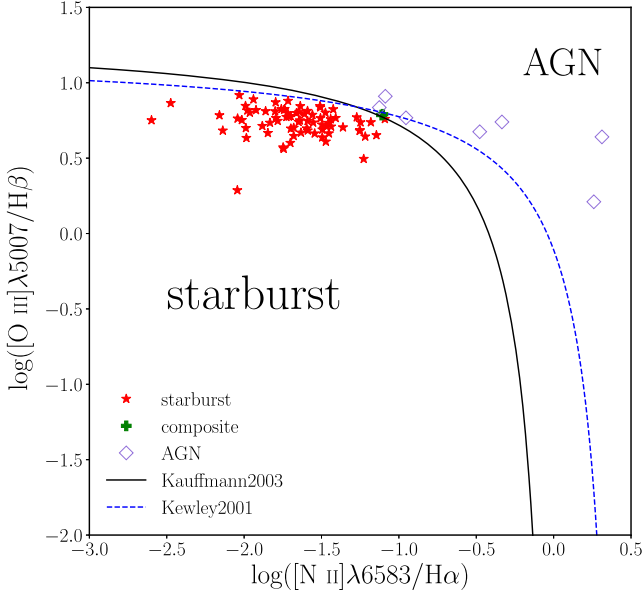


Figure 2. Optical diagnostic diagram (BPT diagram) separating our strong $[\text{O III}]\lambda 5007$ compact galaxies into star-forming galaxies in red stars, composite galaxies in green crosses, and AGNs in purple diamonds. The dashed curve is the theoretical separation limit for star-forming galaxies proposed by Kewley et al. (2001), while the solid curve is the classification lower limit for selecting AGNs proposed by Kauffmann et al. (2003).

luminosity to estimate SFR (Kennicutt 1998):

$$\text{SFR}(M_{\odot} \text{ yr}^{-1}) = 7.9 \times 10^{-42} L_{\text{H}\alpha}(\text{erg s}^{-1}) \quad (1)$$

where the $\text{H}\alpha$ luminosity ($L_{\text{H}\alpha}$) is calculated with the extinction-corrected $\text{H}\alpha$ flux and the luminosity distance from the flat Λ -CDM cosmology. The gas-phase extinction is derived through the Balmer decrement with the assumption of the intrinsic Balmer line ratio of $(\text{H}\alpha/\text{H}\beta)_0 = 2.86$ and the Calzetti et al. (2000) reddening curve. The median gas-phase extinction $E(B - V)$ of our galaxies is about 0.11 mag. The median SFR is about $2.81 M_{\odot} \text{ yr}^{-1}$ with highest value up to $18.38 M_{\odot} \text{ yr}^{-1}$, suggesting that our strong $[\text{O III}]\lambda 5007$ compact galaxies have strong star formation.

3.2. Stellar Mass

The stellar mass is estimated by fitting multiwavelength spectral energy distributions (SEDs) with the stellar population synthesis code of CIGALE (Burgarella et al. 2005; Noll et al. 2009; Boquien et al. 2019). The photometric data include the photometric

magnitudes of SDSS *ugriz*, Dark Energy Spectroscopic Instrument (DESI) *grz*, and WISE W1W2. In CIGALE, we adopt the delayed- τ star-formation history, BC03 (Bruzual & Charlot 2003) stellar population models, Salpeter IMF (Salpeter 1955), nebular emission-line models, Calzetti et al. (2000) reddening curve and dust emission model from Draine et al. (2014). An example of the CIGALE SED fitting (SDSS J154509.39+503448.8) is shown in Figure 4. The stellar mass of our galaxy sample ranges from $7 \times 10^5 M_{\odot}$ to $3 \times 10^9 M_{\odot}$ and the median value is $5 \times 10^7 M_{\odot}$. Most galaxies are low-mass dwarf galaxies.

3.3. Metallicity

There are two widely used methods to measure the gas-phase metallicity of galaxies: one is based on the electron temperature (T_e) (Aller 1984; Gao et al. 2018; Yao et al. 2022) and the other is based on emission-line ratios of strong emission lines (Kobulnicky & Kewley 2004; Pettini & Pagel 2004; Maiolino et al. 2008a). The direct T_e method relies on the detection of $[\text{O III}]\lambda 4363$, which is undetectable in most of our galaxy spectra. We choose N2-based method described in Pettini & Pagel (2004), which is suitable for galaxies with low metallicity:

$$12 + \log(\text{O}/\text{H}) = 8.90 + 0.57 \times \text{N2}, \quad (2)$$

$$\text{N2} \equiv \log\left(\frac{[\text{N II}]\lambda 6583}{\text{H}\alpha}\right) \quad (3)$$

where the calibration is applicable for $-2.5 < \text{N2} < -0.3$. All our galaxies have N2 within this range. The overall metallicity for our galaxy sample is about $\log[\text{O}/\text{H}] + 12 \sim 7.96$. Table 1 lists all the properties of our strong $[\text{O III}]\lambda 5007$ compact galaxies. Note that the errors of SFR and metallicity in this table are propagated from the uncertainties of emission-line measurements, while the error of stellar mass is provided by the CIGALE SED fitting.

4. Results and Discussions

4.1. $EW([\text{O III}])$ versus SFR

Figure 5 shows the equivalent widths of $[\text{O III}]\lambda 5007$ versus SFR of our galaxies. The plot is color-coded by redshift. In this plot, we also present the green-pea galaxies of Cardamone et al. (2009) and Brunker et al. (2020) for comparisons. To exhibit the difference between the strong $[\text{O III}]\lambda 5007$ compact galaxies and normal star-forming galaxies, we randomly select 2000 $\text{H}\alpha$ -detected galaxies with $\text{S}/\text{N} > 5$ from eBOSS whose redshifts are in the same range of our sample. From Figure 5, we can see that our strong $[\text{O III}]\lambda 5007$ galaxies at $0.112 < z < 0.36$ occupy the

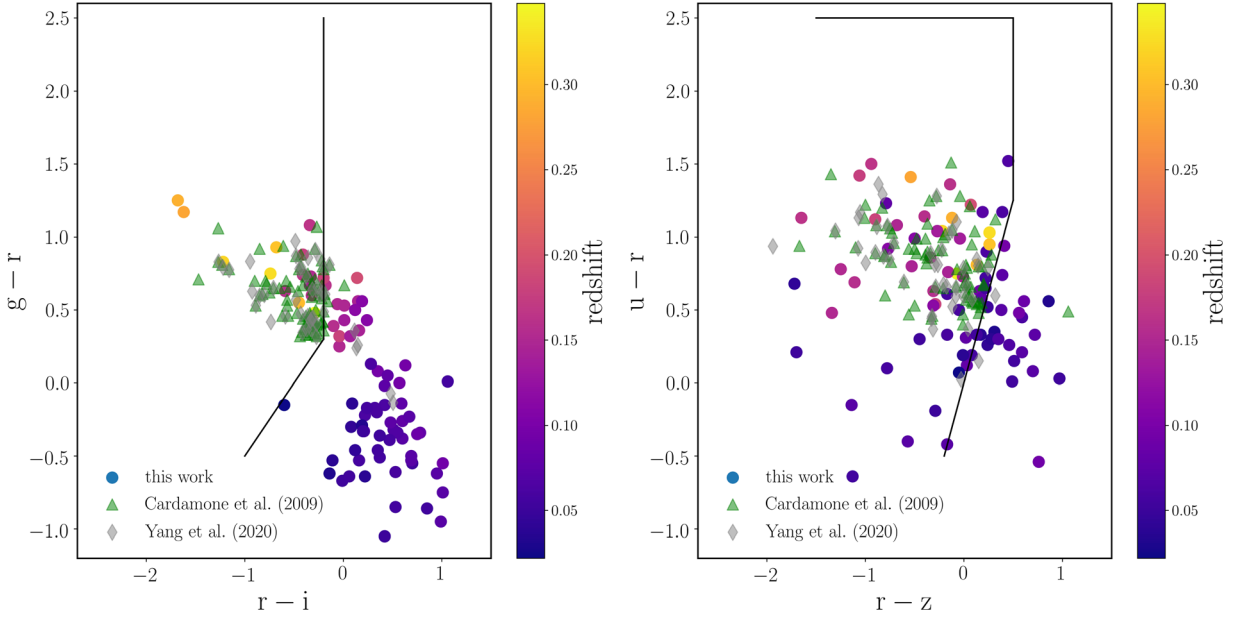


Figure 3. Left: color-color diagram of $r - i$ vs. $g - r$ for our galaxy sample colored by redshift. Right: color-color diagram of $r - z$ vs. $u - r$. Green-pea galaxies from Cardamone et al. (2009; green triangles) and Yang et al. (2017a; gray diamonds) are also overplotted. The solid lines mark the color selection criteria in Cardamone et al. (2009).

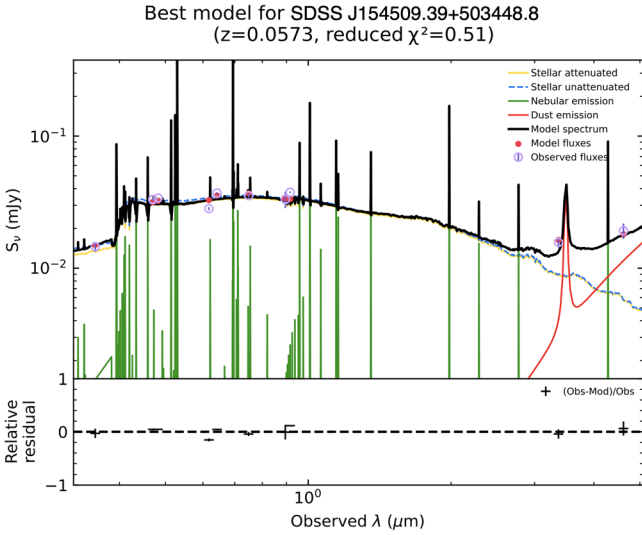


Figure 4. A SED-fitting example using CIGALE with the SDSS $ugriz$ DESI grz and WISE $W1, W2$ photometry. This plot is generated by CIGALE, where the upper panel shows the models and photometric data and the bottom panel presents the residual between the observed and model data.

same region as green-pea galaxies of Cardamone et al. (2009) and Brunner et al. (2020), whose SFR is around $14 M_{\odot} \text{ yr}^{-1}$. Our galaxies at lower redshift present lower SFRs, which is about 24 times less than green-pea galaxies. They are low-redshift counterparts of green-pea galaxies. Meanwhile, there is almost no overlap between our and $H\alpha$ -detected galaxies, indicates that the strong $[\text{O III}]\lambda 5007$ compact galaxies are extremely rare in the low-redshift universe.

4.2. Star-forming Main Sequence

Figure 6 demonstrates the relation between the stellar mass and SFR, which is also known as star-forming main sequence (SFMS; Speagle et al. 2014). The SFR increases steadily with the redshift. In this figure, we also present blueberry galaxies from Yang et al.

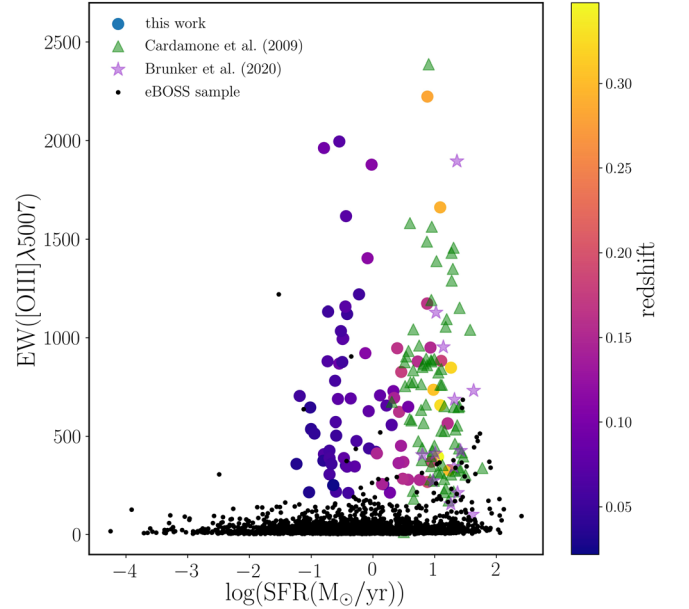


Figure 5. $[\text{O III}]\lambda 5007$ equivalent width against SFR color-coded by redshift. Green-pea galaxies from Cardamone et al. (2009; green triangles), Brunner et al. (2020; purple stars), and eBOSS $H\alpha$ -detected star-forming galaxies (black dots) are also plotted.

(2017b), green-pea galaxies from Cardamone et al. (2009); Yang et al. (2017a) and Brunner et al. (2020). It can be seen that our galaxy sample covers the whole main sequence of both green-pea and blueberry galaxies. They seem to lie in the same sequence, confirming that they are likely to belong to the same type of galaxies but at different redshifts. The robust linear fitting to the main sequence of our galaxies is expressed as:

$$\log(\text{SFR}) = 0.79 \log M_* - 6.48. \quad (4)$$

We also perform a robust linear fitting to all galaxies shown in Figure 6, giving $\log(\text{SFR}) = 0.78 \log M_* - 6.21$. There is no significant difference between these two linear fittings.

We also compare our main-sequence relation with the one for normal star-forming galaxies from Speagle et al. (2014), which is expressed as:

$$\log \text{SFR}(M_*, t) = (0.84 \pm 0.02 - 0.026 \pm 0.003t) \log M_* - (6.51 \pm 0.24 - 0.11 \pm 0.03t), \quad (5)$$

where t is the age of the universe in Gyr. The normal main sequence at $z = 0.11$ (the median redshift of our sample) is overplotted in Figure 6. It is evident that our galaxies show much higher SFR at specified stellar mass. Similar to the results in Cardamone et al. (2009) and Liu et al. (2022), our strong strong [O III] λ 5007 galaxies also have much higher specific SFR (sSFR). In addition, the main-sequence slope of normal galaxies (Speagle et al. 2014) is smaller than ours, implying that strong [O III] λ 5007 compact galaxies possibly have different mass assembly and evolution history. They assemble their mass faster. We also present the galaxies in the epoch of reionization (EoR) from Tacchella et al. (2022) in Figure 6. From this figure, we can see that most of EoR galaxies are located close to the main sequence of our samples at high-mass end, showing the high SFMS consistency. It suggests that our strong [O III] λ 5007 compact galaxies are likely analogous to those high-redshift EoR galaxies.

4.3. Mass–Metallicity Relation

The mass–metallicity relation (MZR) suggests that more massive galaxies tend to be more metal-rich, and the trend holds from local to distant universe (e.g., Lequeux et al. 1979; Tremonti et al. 2004; Maiolino et al. 2008b). Figure 7 shows the MZR of our galaxy sample. The median metallicities in several mass bins are calculated, which are plotted in cyan. For comparisons, the local MZR from the stacked spectra by Andrews & Martini (2013) is presented in blue solid line, while the MZR for star-forming galaxies at $z < 0.3$ and $0.3 < z < 0.5$ derived by Ly et al. (2016) are shown in yellow and green solid lines, respectively. We also compare our MZR with those of other strong [O III] λ 5007 sample as mentioned before. In order for consistent comparison, the metallicity of green-pea galaxies in Cardamone et al. (2009) is recalculated using the same N2-based method as used in this paper. Brunner et al. (2020) uses the O3N2 method to calculate the gas-phase metallicity and Yang et al. (2017b) and Yang et al. (2017a) uses the direct T_e method. As shown in Figure 7, our compact galaxies together with other strong strong [O III] λ 5007 sample present a much flatter MZR comparing to the local MZR. Our MZR is similar to the relation in Liu et al. (2022), and is close to the one at $0.3 < z < 0.5$ derived by Ly et al. (2016). The flatter MZR indicates that strong [O III] λ 5007 compact galaxies might have slower enrichment and are probably on the early stage of star formation.

4.4. Environment

It was stated in Cardamone et al. (2009) that green-pea galaxies reside in low-density environments. We calculate the local density for each galaxy in our sample in the 3D cosmological space, which is the number of neighbor galaxies within a distance of

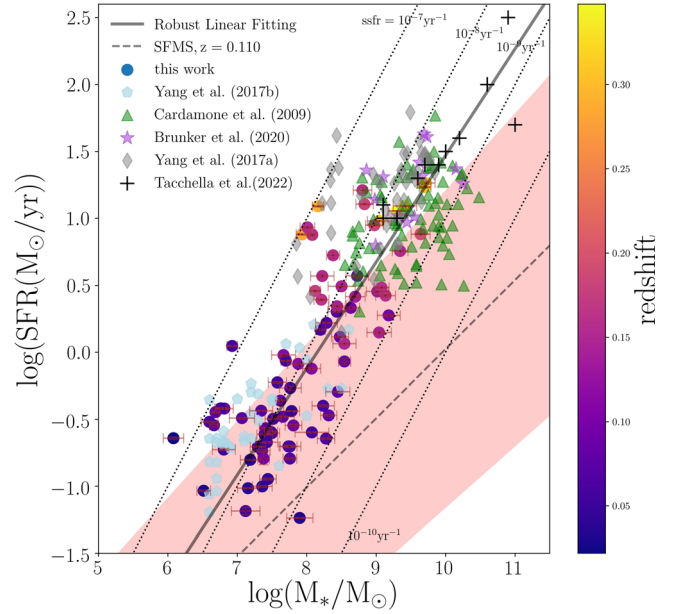


Figure 6. Relation between stellar mass and SFR for our strong [O III] λ 5007 compact galaxies (filled circles) color-coded by redshift. The error bars in orange show the measurement uncertainties. Blueberry galaxies (light blue pentagons) from Yang et al. (2017b), green-pea galaxies from Cardamone et al. (2009; green triangles), Brunner et al. (2020; purple stars), Yang et al. (2017a; gray diamonds), and Tacchella et al. (2022; black cross) are also overplotted. The star-forming main sequence for normal galaxies at redshift of $z = 0.11$ from Speagle et al. (2014) is plotted in dashed line for comparison and the red shade indicates the uncertainty of this SFMS. The solid line represents the best robust linear fitting to our galaxy sample. The dotted lines present the constant sSFRs of 10^{-7} , 10^{-8} , 10^{-9} , and 10^{-10} yr^{-1} .

10 Mpc. A control galaxy sample is randomly selected from eBOSS, including typical star-forming galaxies in the same redshift range of our galaxies. Figure 8 shows the cumulative probability distribution (CDF) of the local density for our galaxy sample and that of the control sample. The CDF of our sample lies above the one of the comparison sample, suggesting that strong [O III] λ 5007 compact galaxies inhabit low-density regions.

5. Summary

In this paper, we have assembled a new set of 76 strong [O III] λ 5007 compact galaxies from SDSS DR16 that spans a redshift range of $0.02 < z < 0.35$. They share common properties with previously studied rare galaxies in the local universe: green-pea and blueberry galaxies. All of these galaxies are compact and have extremely strong [O III] λ 5007, but cover different redshift ranges, so they should have the same physical origin and evolution. We explore their detailed properties with the eBOSS spectra and multiwavelength data, including scaling relations and environment etc. The main conclusion of this paper is as follows.

1. Our strong [O III] λ 5007 compact galaxies present relatively high SFRs (median $\sim 2.81 M_\odot \text{yr}^{-1}$), low stellar mass (median $\log M_* \sim 7.98$) and low metallicity (median $\log[\text{O}/\text{H}] + 12 \sim 7.96$). Their abnormally large equivalent widths of [O III] λ 5007 make them sufficiently different from normal star-forming galaxies.
2. In all diagnostic diagrams including EW([O III]) versus SFR, mass–metallicity relation, and main sequence, the galaxies at $0.112 < z < 0.36$ in our sample have the same properties of green-pea galaxies and those at lower redshift share common properties with blueberry galaxies. It

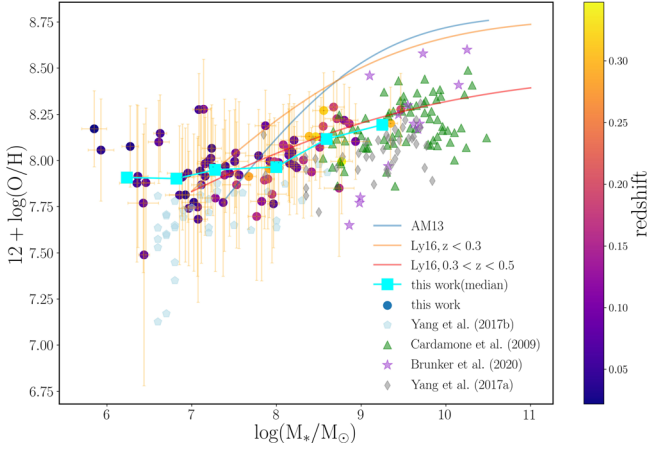


Figure 7. Mass–metallicity relation of our strong [O III] λ 5007 compact galaxies (circles) color-coded by redshift. The orange error bars represent the measurement uncertainties. The other points are the same as those in Figure 6. The cyan squares display the median metallicities in different mass bins. The blue solid curve is the MZR from Andrews & Martini (2013). The yellow and green solid curves are MZRs from Ly et al. (2016) in different redshift ranges.

indicates that such previous studied compact galaxies follow the same physical origin and evolutionary path.

3. From the main-sequence relation, we show that the SFR of our sample increases with redshift. For specified stellar mass, the SFR and corresponding sSFR are higher than those of normal star-forming galaxies. In addition, the slope of the main-sequence relation for our galaxies is about 0.69, higher than that of normal galaxies, indicating strong [O III] λ 5007 compact galaxies assemble their stellar mass faster.
4. The MZR diagram shows most of our galaxies are metal-poor. It has a much shallower slope than those of normal galaxies in local universe. Our MZR is close to the one derived by Ly et al. (2016) at a higher redshift range. The flatter MZR implies that strong [O III] λ 5007 compact galaxies have slower chemical enrichment relative to those normal galaxies at the same redshift and hence are on the earlier stage of the galaxy evolution.
5. The local density is calculated for each compact galaxy in our sample. In contrast to the control sample randomly selected from SDSS DR16, we confirm that our strong [O III] λ 5007 compact galaxies reside in relatively low-density environment.

Ongoing large-scale spectroscopic surveys, such as DESI (DESI Collaboration et al. 2016), will provide great

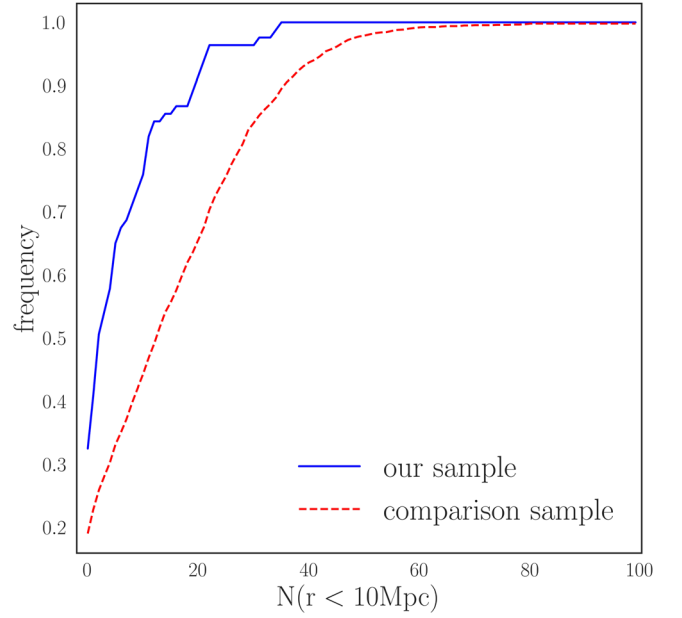


Figure 8. Cumulative probability distribution of the local density for our galaxies (solid blue line) and that of a comparison sample (dashed red line).

opportunities for thoroughly understanding such compact galaxies with extremely strong characteristic emission lines.

Acknowledgments

This work is supported by the National Natural Science Foundation of China (NSFC; Nos. 12120101003 and 11890691), National Key R&D Program of China (grant No. 2022YFA1602902), and Beijing Municipal Natural Science Foundation (grant No. 1222028). This work is also supported by the China Manned Space Project (Nos. CMS-CSST-2021-A02 and CMS-CSST-2021-A04). X.K. acknowledges the supports from the Strategic Priority Research Program of Chinese Academy of Sciences (No. XDB 41000000), NSFC (Nos.12233008 and 11973038), China Manned Space Project (Grant No. CMS-CSST-2021-A07), the Cyrus Chun Ying Tang Foundations and the Frontier Scientific Research Program of Deep Space Exploration Laboratory.

Appendix Properties of Our Samples

In the Table 1, we present all the properties of our strong [O III] λ 5007 compact galaxies discussed in the Section 3.

Table 1
Properties of our Compact Galaxies with Strong [O III] λ 5007 Emission

SDSS ID	R.A. (J2000)	Decl. (J2000)	Redshift	$\log L(H\alpha)$ (erg s^{-1})	EW([O III]) (\AA)	SFR ($M_{\odot} \text{ yr}^{-1}$)	$\log (M_{*}/M_{\odot})$	12+ $\log(\text{O}/\text{H})$
(1)	(2)	(3)	(4)	(5)	(6)	(7)	(8)	(9)
SDSS J081136.31+304311.1	122.90131	30.71977	0.1575	41.83	878.98	5.31 ± 0.29	8.11 ± 0.09	8.06 ± 0.25
SDSS J164348.57+343935.6	250.95239	34.65991	0.1102	40.98	921.21	0.75 ± 0.01	7.82 ± 0.13	7.78 ± 0.43
SDSS J013425.48+084939.8	23.60620	8.82772	0.0518	40.38	1132.45	0.19 ± 0.00	6.80 ± 0.17	7.81 ± 0.38
SDSS J011720.17+073145.0	19.33406	7.52919	0.2818	41.98	2223.96	7.62 ± 0.09	7.71 ± 0.09	7.91 ± 0.28
SDSS J084022.58+214109.5	130.09411	21.68599	0.1375	41.56	451.49	2.85 ± 0.03	8.51 ± 0.16	7.94 ± 0.24
SDSS J022635.74-011021.5	36.64893	-1.17264	0.0962	41.38	121.92	1.89 ± 0.04	8.72 ± 0.17	8.10 ± 0.21
SDSS J080942.74+491821.1	122.42809	49.30587	0.0781	41.03	626.04	0.85 ± 0.05	8.18 ± 0.09	7.96 ± 0.25
SDSS J083745.20+375237.8	129.43834	37.87718	0.1615	41.53	622.60	2.65 ± 0.06	8.73 ± 0.14	8.23 ± 0.21
SDSS J112624.43-005449.0	171.60182	-0.91362	0.0772	40.74	690.69	0.44 ± 0.00	7.37 ± 0.02	7.77 ± 0.40
SDSS J151806.17+264617.8	229.52574	26.77163	0.0829	41.22	706.35	1.30 ± 0.02	7.93 ± 0.12	8.19 ± 0.19
SDSS J155239.84+170851.2	238.16603	17.14758	0.0721	40.62	993.21	0.32 ± 0.01	6.84 ± 0.18	7.77 ± 0.38
SDSS J153126.82+203027.4	232.86176	20.50763	0.0657	40.31	408.72	0.16 ± 0.00	7.56 ± 0.10	7.93 ± 0.34
SDSS J152826.52+231843.1	232.11053	23.31198	0.0595	41.27	255.62	1.47 ± 0.02	7.88 ± 0.07	7.76 ± 0.24
SDSS J234452.01-005130.0	356.21674	-0.85835	0.3003	42.34	327.01	17.12 ± 0.14	9.33 ± 0.08	8.20 ± 0.20
SDSS J011755.46-001249.5	19.48110	-0.21375	0.1923	41.99	267.44	7.64 ± 0.07	9.43 ± 0.14	8.28 ± 0.20
SDSS J025349.27+030100.6	43.45530	3.01685	0.0724	40.62	996.21	0.33 ± 0.00	7.45 ± 0.16	7.92 ± 0.40
SDSS J234916.37+043000.1	357.31822	4.50003	0.0667	40.37	880.01	0.18 ± 0.00	7.01 ± 0.12	7.87 ± 0.42
SDSS J224750.52+040721.4	341.96051	4.12262	0.0378	40.30	375.70	0.16 ± 0.00	6.86 ± 0.14	7.91 ± 0.29
SDSS J083516.74+114122.0	128.81979	11.68945	0.0583	40.49	780.82	0.24 ± 0.00	7.04 ± 0.11	7.91 ± 0.32
SDSS J075321.62+095344.0	118.34012	9.89556	0.0719	40.67	1617.05	0.37 ± 0.00	7.07 ± 0.16	7.75 ± 0.37
SDSS J112945.62+355107.0	172.44012	35.85195	0.0561	40.40	426.83	0.20 ± 0.00	7.04 ± 0.11	7.68 ± 0.45
SDSS J120557.30+025656.5	181.48878	2.94904	0.0766	40.81	346.29	0.51 ± 0.01	8.01 ± 0.17	8.03 ± 0.25
SDSS J114653.25+034241.9	176.72189	3.71165	0.0447	40.66	351.80	0.36 ± 0.00	7.41 ± 0.11	8.07 ± 0.24
SDSS J111547.88+071910.2	168.94953	7.31952	0.0619	40.50	571.16	0.25 ± 0.01	7.11 ± 0.11	8.01 ± 0.27
SDSS J224953.77+164659.9	342.47407	16.78331	0.0882	40.56	868.13	0.28 ± 0.01	7.44 ± 0.12	8.04 ± 0.29
SDSS J225113.60+095512.4	342.80668	9.92013	0.0332	39.86	359.21	0.06 ± 0.00	7.01 ± 0.19	7.81 ± 0.36
SDSS J161221.60+110516.4	243.09003	11.08790	0.0722	41.32	654.65	1.66 ± 0.02	8.01 ± 0.16	8.11 ± 0.20
SDSS J120402.17+072558.6	181.00906	7.43296	0.0322	40.07	214.85	0.09 ± 0.00	6.38 ± 0.10	8.08 ± 0.22
SDSS J124018.08+130344.5	190.07535	13.06237	0.0632	40.46	249.97	0.23 ± 0.00	8.20 ± 0.13	7.98 ± 0.28
SDSS J140153.86+123349.8	210.47442	12.56386	0.0619	40.84	475.77	0.54 ± 0.02	7.52 ± 0.16	8.00 ± 0.28
SDSS J145425.33+121221.6	223.60555	12.20601	0.1508	41.67	278.82	3.72 ± 0.09	7.89 ± 0.17	7.82 ± 0.37
SDSS J000441.90+132012.4	1.17459	13.33678	0.0548	40.61	876.37	0.32 ± 0.00	7.02 ± 0.12	7.74 ± 0.31
SDSS J091819.28+305654.8	139.58036	30.94858	0.0946	41.43	728.39	2.15 ± 0.04	8.21 ± 0.12	7.99 ± 0.22
SDSS J143251.79+271111.2	218.21581	27.18645	0.0609	40.40	305.83	0.20 ± 0.00	7.54 ± 0.16	8.03 ± 0.25
SDSS J231521.95+214328.3	348.84148	21.72454	0.0549	40.88	1218.94	0.60 ± 0.01	6.93 ± 0.13	7.91 ± 0.21
SDSS J004954.52+285449.0	12.47719	28.91362	0.0390	40.10	535.40	0.10 ± 0.00	6.87 ± 0.14	7.77 ± 0.37
SDSS J004641.11+300259.1	11.67133	30.04976	0.0426	40.16	513.58	0.11 ± 0.00	7.01 ± 0.12	7.94 ± 0.33
SDSS J101028.98+231259.0	152.62078	23.21641	0.0664	41.41	556.81	2.01 ± 0.04	8.01 ± 0.13	7.97 ± 0.21
SDSS J115907.58+292810.8	179.78162	29.46967	0.0511	40.51	503.12	0.25 ± 0.01	7.13 ± 0.09	7.97 ± 0.26
SDSS J142207.05+505757.1	215.52941	50.96588	0.1813	42.21	882.05	12.76 ± 0.14	8.58 ± 0.13	8.29 ± 0.19
SDSS J154507.90+574702.5	236.28294	57.78404	0.0751	40.54	688.18	0.27 ± 0.00	7.14 ± 0.09	7.98 ± 0.31
SDSS J125930.29+561910.7	194.87624	56.31966	0.0721	40.56	1995.34	0.29 ± 0.01	6.48 ± 0.07	7.49 ± 0.71
SDSS J013411.59-051747.9	23.54832	-5.29665	0.0951	41.67	648.34	3.73 ± 0.04	8.60 ± 0.16	8.22 ± 0.20
SDSS J093355.08+510924.6	143.47951	51.15683	0.2913	42.19	1661.73	12.29 ± 0.13	7.98 ± 0.08	7.96 ± 0.27
SDSS J091216.82+482004.8	138.07011	48.33469	0.3063	42.08	735.10	9.55 ± 0.13	8.75 ± 0.17	8.13 ± 0.24
SDSS J112652.66+460501.3	171.71944	46.08371	0.3476	42.16	395.36	11.33 ± 0.13	8.94 ± 0.13	8.00 ± 0.28
SDSS J124113.49+491143.2	190.30621	49.19536	0.1439	41.45	693.48	2.21 ± 0.03	8.07 ± 0.13	8.07 ± 0.29
SDSS J085503.74+471818.5	133.76561	47.30515	0.1585	42.31	564.37	16.22 ± 0.85	8.44 ± 0.13	8.00 ± 0.32
SDSS J221042.80+184324.2	332.67834	18.72339	0.0784	40.63	389.13	0.34 ± 0.01	8.04 ± 0.12	8.00 ± 0.26
SDSS J004213.42+231047.2	10.55592	23.17978	0.0575	40.50	217.95	0.25 ± 0.00	7.18 ± 0.24	7.93 ± 0.27
SDSS J004221.14+252353.1	10.58809	25.39808	0.1438	41.25	256.71	1.40 ± 0.04	8.54 ± 0.18	7.85 ± 0.37
SDSS J014137.14+275018.5	25.40477	27.83850	0.0586	40.58	1033.71	0.30 ± 0.00	6.45 ± 0.12	7.91 ± 0.38
SDSS J000115.81+270025.1	0.31589	27.00699	0.0922	40.31	1962.18	0.16 ± 0.02	7.15 ± 0.08	8.28 ± 0.27
SDSS J233648.13+264338.5	354.20056	26.72737	0.1642	41.50	946.34	2.47 ± 0.04	8.00 ± 0.11	7.99 ± 0.24
SDSS J231123.10+245547.3	347.84628	24.92981	0.1454	41.60	369.21	3.12 ± 0.02	8.34 ± 0.20	8.09 ± 0.22
SDSS J221955.10+303036.6	334.97959	30.51017	0.1760	41.56	825.83	2.88 ± 0.04	7.92 ± 0.08	7.90 ± 0.27
SDSS J021442.13+313608.0	33.67555	31.60223	0.0538	39.92	703.59	0.07 ± 0.00	6.69 ± 0.21	7.88 ± 0.43
SDSS J023526.26+020638.2	38.85943	2.11061	0.0220	40.46	251.63	0.23 ± 0.01	5.85 ± 0.15	8.17 ± 0.21
SDSS J013808.83-001933.6	24.53682	-0.32600	0.0562	41.15	420.95	1.11 ± 0.01	6.68 ± 0.08	8.15 ± 0.21
SDSS J112608.24+575531.8	171.53436	57.92553	0.1807	42.05	370.44	8.87 ± 0.11	8.84 ± 0.13	8.19 ± 0.20
SDSS J135716.14+555310.4	209.31727	55.88624	0.0373	40.09	644.94	0.10 ± 0.00	6.51 ± 0.15	8.06 ± 0.28
SDSS J135613.67+521945.5	209.05699	52.32931	0.1115	41.08	1877.47	0.95 ± 0.03	7.27 ± 0.17	7.92 ± 0.41

Table 1
(Continued)

SDSS ID	R.A. (J2000)	Decl. (J2000)	Redshift	$\log L(H\alpha)$ (erg s^{-1})	EW([O III]) (\AA)	SFR ($M_{\odot} \text{ yr}^{-1}$)	$\log (M_{*}/M_{\odot})$	12+log(O/H)
(1)	(2)	(3)	(4)	(5)	(6)	(7)	(8)	(9)
SDSS J132116.78+513926.8	200.31992	51.65745	0.1517	41.86	277.89	5.72 ± 0.08	8.77 ± 0.11	8.20 ± 0.20
SDSS J125701.58+595401.0	194.25662	59.90030	0.0590	40.40	388.64	0.20 ± 0.00	7.38 ± 0.12	7.99 ± 0.28
SDSS J130735.50+520221.7	196.89796	52.03939	0.1523	42.03	949.86	8.55 ± 0.13	7.85 ± 0.10	7.70 ± 0.35
SDSS J075742.06+451846.2	119.42526	45.31285	0.0546	41.04	438.05	0.86 ± 0.01	7.06 ± 0.07	8.28 ± 0.19
SDSS J123548.35+434221.5	188.95150	43.70599	0.3197	42.37	847.41	18.38 ± 0.53	8.51 ± 0.13	8.27 ± 0.20
SDSS J131829.29+444909.1	199.62205	44.81920	0.1574	41.59	284.00	3.05 ± 0.04	8.64 ± 0.11	8.13 ± 0.22
SDSS J132653.76+435741.9	201.72401	43.96167	0.1386	41.52	363.34	2.60 ± 0.07	8.43 ± 0.14	8.07 ± 0.22
SDSS J154509.39+503448.8	236.28915	50.58024	0.0573	40.70	211.47	0.40 ± 0.01	8.02 ± 0.16	8.05 ± 0.25
SDSS J142053.29+575442.7	215.22206	57.91187	0.0534	40.43	359.26	0.21 ± 0.00	7.31 ± 0.16	7.97 ± 0.25
SDSS J144359.00+462106.4	220.99587	46.35179	0.1496	41.17	412.84	1.16 ± 0.01	8.01 ± 0.17	7.87 ± 0.34
SDSS J152352.63+425157.0	230.96931	42.86583	0.3260	42.19	656.16	12.38 ± 0.12	8.74 ± 0.17	8.13 ± 0.24
SDSS J163845.33+412432.9	249.68889	41.40916	0.0727	40.68	345.42	0.38 ± 0.00	6.67 ± 0.12	8.10 ± 0.23
SDSS J121823.93+392508.7	184.59971	39.41910	0.0510	40.68	1120.17	0.38 ± 0.01	6.60 ± 0.09	7.91 ± 0.25
SDSS J124845.07+401913.8	192.18782	40.32053	0.0716	40.66	1157.42	0.36 ± 0.00	6.49 ± 0.05	7.88 ± 0.40
SDSS J133107.26+363337.9	202.78029	36.56054	0.1143	41.02	1402.93	0.82 ± 0.01	7.25 ± 0.15	7.80 ± 0.40
SDSS J212827.39+000822.3	322.11413	0.13953	0.1645	41.98	1172.76	7.55 ± 0.15	7.85 ± 0.03	7.89 ± 0.26

Note. (1) Object name; (2–3) R.A. and decl. in J2000 from SDSS DR16; (4) SDSS spectroscopic redshift; (5) logarithmic $H\alpha$ luminosity in erg s^{-1} ; (6) [O III] equivalent width in \AA ; (7) Star-formation rate estimated from $H\alpha$ in $M_{\odot} \text{ yr}^{-1}$; (8) logarithmic stellar mass in M_{\odot} ; (9) metallicity estimated with the [N II] line.

ORCID iDs

Weiyu Ding  <https://orcid.org/0000-0003-0230-4596>

Hu Zou  <https://orcid.org/0000-0002-6684-3997>

Xu Kong  <https://orcid.org/0000-0002-7660-2273>

Yulong Gao  <https://orcid.org/0000-0002-5973-694X>

Fujia Li  <https://orcid.org/0000-0001-9472-2052>

Jie Song  <https://orcid.org/0000-0002-0846-7591>

Jundan Nie  <https://orcid.org/0000-0001-6590-8122>

References

- Ahumada, R., Prieto, C. A., Almeida, A., et al. 2020, *ApJS*, 249, 3
- Aller, L. H. 1984, *Physics of Thermal Gaseous Nebulae* (Dordrecht: Reidel)
- Andrews, B. H., & Martini, P. 2013, *ApJ*, 765, 140
- Baldwin, J. A., Phillips, M. M., & Terlevich, R. 1981, *PASP*, 93, 5
- Blanton, M. R., Bershad, M. A., Abolfathi, B., et al. 2017, *AJ*, 154, 28
- Boquien, M., Burgarella, D., Roehly, Y., et al. 2019, *A&A*, 622, A103
- Brunker, S. W., Salzer, J. J., Janowiecki, S., Finn, R. A., & Helou, G. 2020, *ApJ*, 898, 68
- Bruzual, G., & Charlot, S. 2003, *MNRAS*, 344, 1000
- Burgarella, D., Buat, V., & Iglesias-Páramo, J. 2005, *MNRAS*, 360, 1413
- Calzetti, D., Armus, L., Bohlin, R. C., et al. 2000, *ApJ*, 533, 682
- Cardamone, C., Schawinski, K., Sarzi, M., et al. 2009, *MNRAS*, 399, 1191
- Cid Fernandes, R., Mateus, A., Sodré, L., Stasińska, G., & Gomes, J. M. 2005, *MNRAS*, 358, 363
- Dawson, K. S., Schlegel, D. J., Ahn, C. P., et al. 2013, *AJ*, 145, 10
- Dawson, K. S., Kneib, J.-P., Percival, W. J., et al. 2016, *AJ*, 151, 44
- DESI Collaboration, Aghamousa, A., Aguilar, J., et al. 2016, arXiv:1611.00036
- Draine, B. T., Aniano, G., Krause, O., et al. 2014, *ApJ*, 780, 172
- Fan, X., Strauss, M. A., Becker, R. H., et al. 2006, *AJ*, 132, 117
- Finkelstein, S. L., & Bagley, M. B. 2022, *ApJ*, 938, 25
- Finkelstein, S. L., D'Aloisio, A., Paardekooper, J.-P., et al. 2019, *ApJ*, 879, 36
- Gao, Y., Bao, M., Yuan, Q., et al. 2018, *ApJ*, 869, 15
- Gunn, J. E., Siegmund, W. A., Mannery, E. J., et al. 2006, *AJ*, 131, 2332
- Haiman, Z., & Loeb, A. 1998, *ApJ*, 503, 505
- Henry, A., Scarlata, C., Martin, C. L., & Erb, D. 2015, *ApJ*, 809, 19
- Izotov, Y. I., Guseva, N. G., & Thuan, T. X. 2011, *ApJ*, 728, 161
- Izotov, Y. I., Schaerer, D., Worseck, G., et al. 2020, *MNRAS*, 491, 468
- Jiang, T., Malhotra, S., Rhoads, J. E., & Yang, H. 2019, *ApJ*, 872, 145
- Kauffmann, G., Heckman, T. M., Tremonti, C., et al. 2003, *MNRAS*, 346, 1055
- Kennicutt, R. C. J. 1998, *ARA&A*, 36, 189
- Kewley, L. J., Dopita, M. A., Sutherland, R. S., Heisler, C. A., & Trevena, J. 2001, *ApJ*, 556, 121
- Kobulnicky, H. A., & Kewley, L. J. 2004, *ApJ*, 617, 240
- Lequeux, J., Peimbert, M., Rayo, J. F., Serrano, A., & Torres-Peimbert, S. 1979, *A&A*, 80, 155
- Lintott, C. J., Schawinski, K., Slosar, A., et al. 2008, *MNRAS*, 389, 1179
- Liu, S., Luo, A. L., Yang, H., et al. 2022, *ApJ*, 927, 57
- Ly, C., Malkan, M. A., Nagao, T., et al. 2014, *ApJ*, 780, 122
- Ly, C., Malkan, M. A., Rigby, J. R., & Nagao, T. 2016, *ApJ*, 828, 67
- Madau, P., Rees, M. J., Volonteri, M., Haardt, F., & Oh, S. P. 2004, *ApJ*, 604, 484
- Maiolino, R., Nagao, T., Grazian, A., et al. 2008a, *A&A*, 488, 463
- Maiolino, R., Nagao, T., Grazian, A., et al. 2008b, in *ASP Conf. Ser. 396, Formation and Evolution of Galaxy Disks*, ed. J. G. Funes & E. M. Corsini (San Francisco, CA: ASP), 409
- Malkan, M. A., Scully, S. T., & Stecker, F. W. 2021, *ApJ*, 909, 52
- Markwardt, C. B. 2009, in *ASP Conf. Ser. 411, Astronomical Data Analysis Software and Systems XVIII*, ed. D. A. Bohlender, D. Durand, & P. Dowler (San Francisco, CA: ASP), 251
- McGreer, I. D., Mesinger, A., & D'Odorico, V. 2015, *MNRAS*, 447, 499
- Nakajima, K., & Ouchi, M. 2014, *MNRAS*, 442, 900
- Noll, S., Burgarella, D., Giovannoli, E., et al. 2009, *A&A*, 507, 1793
- Pettini, M., & Pagel, B. E. J. 2004, *MNRAS*, 348, L59
- Rivera-Thorsen, T. E., Hayes, M., Östlin, G., et al. 2015, *ApJ*, 805, 14
- Robertson, B. E., Ellis, R. S., Dunlop, J. S., McLure, R. J., & Stark, D. P. 2010, *Natur*, 468, 49
- Salpeter, E. E. 1955, *ApJ*, 121, 161
- Salzer, J. J., Gronwall, C., Sarajedini, V. L., & Chomiuk, L. B. 2000, *AAS Meeting Abstracts*, 197, 76.06
- Speagle, J. S., Steinhardt, C. L., Capak, P. L., & Silverman, J. D. 2014, *ApJS*, 214, 15
- Tacchella, S., Finkelstein, S. L., Bagley, M., et al. 2022, *ApJ*, 927, 170
- Tremonti, C. A., Heckman, T. M., Kauffmann, G., et al. 2004, *ApJ*, 613, 898
- Veilleux, S., & Osterbrock, D. E. 1987, *ApJS*, 63, 295
- Verhamme, A., Orlitová, I., Schaerer, D., et al. 2017, *A&A*, 597, A13
- Yang, H., Malhotra, S., Rhoads, J. E., & Wang, J. 2017a, *ApJ*, 847, 38
- Yang, H., Malhotra, S., Gronke, M., et al. 2017b, *ApJ*, 844, 171
- Yao, Y., Liu, H., Kong, X., et al. 2022, *ApJ*, 926, 57
- York, D. G., Adelman, J., Anderson, J. E. J., et al. 2000, *AJ*, 120, 1579
- Yung, L. Y. A., Somerville, R. S., Finkelstein, S. L., et al. 2021, *MNRAS*, 508, 2706
- Yung, L. Y. A., Somerville, R. S., Finkelstein, S. L., et al. 2020, *MNRAS*, 496, 4574